ARTICLES
https://doi.org/10.1038/s41567-018-0277-7
nature physics
Corrected: Author Correction

Polygonal motion and adaptable phototaxis via flagellar beat switching in the microswimmer *Euglena gracilis*

Alan C. H. Tsang, Amy T. Lam and Ingmar H. Riedel-Kruse*

Biological microswimmers exhibit versatile strategies for sensing and navigating their environment, such as run-and-tumble and curvature modulation. Here, we report a striking phototactic behaviour of the microswimmer Euglena gracilis, where these eukaryotic cells swim in polygonal trajectories due to a sudden increase in light intensity. While smoothly curved trajectories are common for microswimmers, such quantized ones have not been reported previously. We find that this polygonal behaviour emerges from periodic switching between the flagellar beating patterns of helical swimming and spinning behaviours. We develop and experimentally validate a biophysical model that describes the phase relationship between the eyespot, cell orientation, light detection and cellular reorientation, accounting for all three behavioural states. Coordinated switching between these behaviours selects for ballistic, superdiffusive, diffusive or subdiffusive motion (including tuning the effective diffusion constant over several orders of magnitude), thereby enabling navigation in spatially structured light fields, such as edge avoidance and gradient descent. This feedback control links multiple system scales (flagellar beats, cellular behaviours and phototaxis strategies), with implications for other natural and synthetic microswimmers.

Biological microswimmers exhibit a variety of intricate behaviours and strategies to achieve navigational tasks in response to environmental stimuli such as chemicals[1–3], light[4–6], electric fields[7–9] and fluid flows[10]. Experimental and theoretical studies in many microorganisms (for example, *Escherichia coli*[2], *Chlamydomonas reinhardtii*[11–15], *Euglena gracilis*[6,16–18], *Volvox globator*[4] and *Paramecium caudatum*[7,8]) have elucidated feedback-control mechanisms that tie together three spatiotemporal scales: fast subcellular sensors and actuators operate within tens of milliseconds, leading to cellular reorientation behaviours typically within 1 s, ultimately resulting in directed cell movement and task accomplishment over tens of seconds[1,19,20]. Many microswimmers ('chiral microswimmers') roll around their body axis, leading to helical swimming[12,21], with external stimuli causing smooth curvature modulation[3,12,21] or intermittent, randomized body reorientation ('tumbling')[2,20].

Polygonal trajectories following increased light intensity

In contrast, here we report striking polygonal swimming trajectories in *Euglena gracilis* (Fig. 1a(i)–(iii) and Supplementary Video 1), where cells alternate between helical swimming and sharp turning with well-defined lengths and angles, respectively. These polygons emerge within ~1 s after a sudden 6–20-fold step-up in light intensity from ~50 lx to ~300–1,000 lx. These trajectories are approximately confined to a plane perpendicular to the light stimulus, have a clockwise handedness (when observed from the direction opposite the light source) and they are not due to surface interactions as they also occur deep inside the fluid. Turning angles range from 30° to 150° yielding polygons from order 3 upwards (Fig. 1a(i)–(iii)); these angles also decrease over time as cells adapt to the increased light level, thereby leading to increased polygon order and also polygonal spirals. After $\gtrsim$20 turns, cells intermittently skip polygonal turns, eventually transitioning back to pure helical motion after ~1 min.

Euglena are of wide interest for biophysics and biochemistry research[5,6,17,18,22–24], education[25–30], biosensing[31], biocomputation[32,33], and food, chemical and fuel production[34]; being part of an outgroup to much eukaryotic life promises impactful discoveries[34,35]. *Euglena* are single-celled microorganisms with ellipsoidal bodies of length $l \sim 50\,\mu\text{m}$ and width $w \sim 5\,\mu\text{m}$. They swim at $v \sim 50\text{–}100\,\mu\text{m}\,\text{s}^{-1}$ while rolling around their long axis anticlockwise (as seen from behind) at a frequency of $\omega \sim 1\text{–}2\,\text{Hz}$[5,6]. Their single flagellum beats at $\Omega \sim 20\text{–}40\,\text{Hz}$[18,36] (15–20 beats per roll). *Euglena* are known to exhibit versatile behaviours. For example, they swim along helical paths (Fig. 1b and Supplementary Video 2) at weak light intensities (~100 lx)[6], or spinning locally (Fig. 1c and Supplementary Video 3) at high light intensities (>3,000 lx)[22]. Other behaviours include transient freezing[22] and body deformations[24], but they are not relevant here. *Euglena* sense light signals via a photoreceptor that is partially shaded by the stigma (red 'eyespot', Fig. 1d)[5]. This signal is converted into different three-dimensional (3D) flagellar beating patterns depending on light intensity[23], which determines swimming speed, rolling frequency, and sideways turning[5]. These motions change the cell orientation and position in 3D space, which in turn affects the detected light signal[6]. This complex feedback enables *Euglena* to adjust their swimming paths and phototaxis strategies in accordance to light conditions, such as positive and negative phototaxis[5,6,27,37] or avoidance turning at light barriers[25,33]

Due to the novelty of the observed polygonal behaviour, we further investigate its origins and characteristics. We investigated its dependence on light intensity by stepping up the microscope light from ~50 lx to various higher intensities (Fig. 1e). The obtained distributions reveal three behavioural states ($n = 33$ cells; Fig. 1f) with the polygonal behaviour forming a transition between helical swimming and spinning at intermediate light levels. In the following, we describe the basis of this polygonal behaviour and its relationship to helical and spinning behaviours (Fig. 1b,c) at the levels of flagellar beats (Figs. 2 and 3), swimming behaviours (Figs. 4 and 5) and phototaxis strategies (Fig. 6).

Department of Bioengineering, Stanford University, Stanford, CA, USA. *e-mail: ingmar@stanford.edu

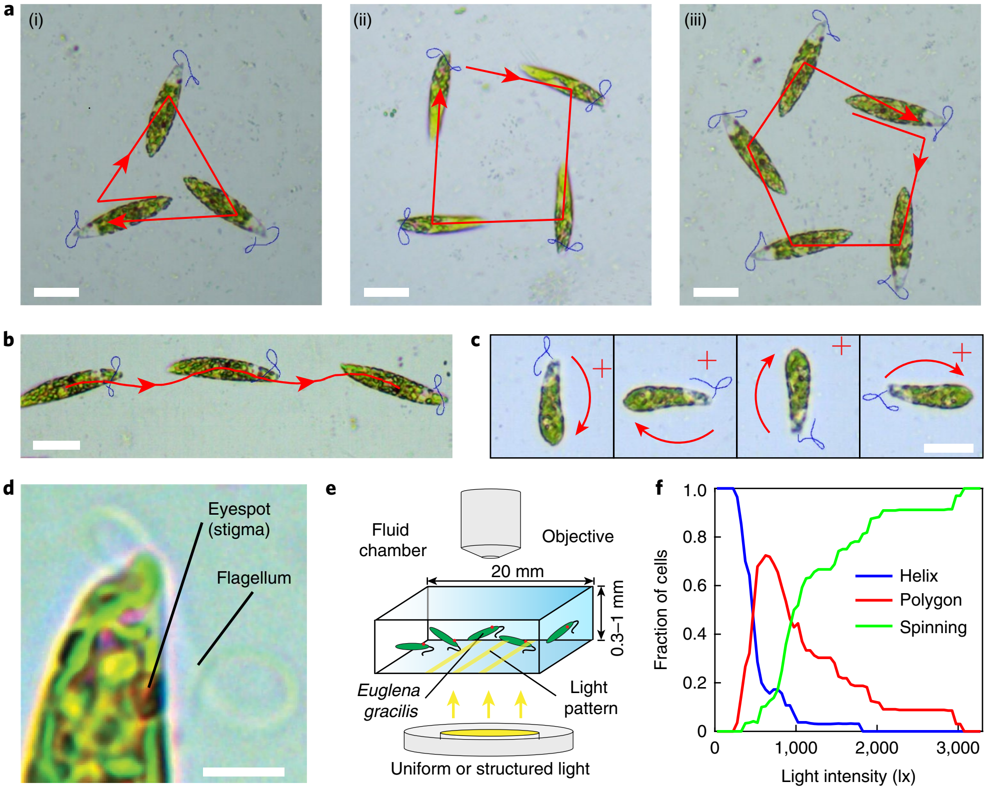

Fig. 1 | *Euglena gracilis* cells swim in striking polygonal patterns following a step-up in light intensity. a, *Euglena* cells exhibit polygonal swimming trajectories of various orders. (i–iii) Polygonal trajectories with order 3–5. **b**,**c**, These polygonal behaviours are distinct from the known behaviours of helical swimming (**b**) and localized spinning (**c**). The red plus symbols mark the same spatial location in the images. Flagellum outlines are traced and coloured in blue. Duration of motion in **a**(i), **a**(ii), **a**(iii), **b** and **c**: 2 s, 2.2 s, 4.1 s, 1.35 s, 0.65 s. **d**, *Euglena* has a red 'eyespot' that shades its photoreceptor. The cell rolls, swims and turns due to its flagellar beating. This beat is affected by the light intensity sensed by the photoreceptor. **e**, A schematic of the experimental set-up: cells are illuminated from below by either uniform or structured light through the microscope lamp or a projector, respectively. Unless otherwise specified, uniform light field is applied. **f**, We observed three behavioural states of *Euglena* following a step-up to various light intensities (always starting from weak light of ~50 lx; $n = 33$ cells): polygonal behaviour appears at intermediate light intensities between helical and spinning behaviours. Scale bars, 20 µm (**a**–**c**) and 5 µm (**d**).

Periodic switching between distinct flagellar beat patterns

First, we investigated at the subcellular level what flagellar beat patterns generate polygonal swimming, and how those beat patterns relate to those of helical swimming and spinning (Fig. 2). We manually tracked the flagellum outlines ($n = 3$ cells for >1.4 s for each behaviour, sampling rate 200 fps, ~40 beat cycles, ~7 beat patterns per cycle, ~3,000 frames total; Supplementary Fig. 3 and Supplementary Section 3.2). All three behavioural states showed distinct flagellar beat patterns (Fig. 2a–d and Supplementary Video 4). During helical swimming, the flagellum twists into two loops that are distributed on both sides of the cell (Fig. 2a), whereas for spinning, the flagellum twists into one loop extending towards the front of the cell and bends to the side opposite to the turning direction (Fig. 2b). Polygonal swimming emerges from periodic switching between two beat patterns that resemble those of helical swimming (Fig. 2c) and spinning (Fig. 2d), which coincides with the swimming and turning phases of the polygon, respectively.

To quantify these beat patterns over time, we measured their instantaneous maximum vertical distance f_1 and mean horizontal distance f_2 (positive on the cell's right side from a top-down view) from the cell tip, as well as the cell orientation ϕ, from their 2D projection (Fig. 2e). While this approach neglects many 3D aspects of flagellar beating, it is sufficient for the following analysis (Supplementary Section 3.2). For helical beat patterns, f_1 remains small (<3 µm), f_2 oscillates around 0 µm and ϕ stays nearly constant (Fig. 2f). In contrast, spinning beat patterns have large f_1 (~6 µm), negative f_2 and significantly decreasing ϕ over time (Fig. 2g). The asymmetry in f_2 may explain why this beat pattern leads to turning rather than forward motion. For polygonal behaviour, f_1, f_2 and the change in ϕ reveal two distinct beat patterns (Fig. 2h) that closely resemble those of helical and spinning motions (Fig. 2f,g), occurring during the straight swimming and turning phases, respectively (Supplementary Section 3.2). However, closer inspection of the eyespot reveals that during polygonal turning, cells still roll around their long axis, while during spinning they do not (Supplementary Videos 1 and 3 and Supplementary Fig. 4). This implies that there are subtle differences in these beat patterns. Thus, we conclude that the beat patterns for helical swimming and spinning have distinct geometric characteristics, and polygonal swimming emerges to first approximation via switching between both beat patterns (Fig. 2i).

We then assessed how the number of spinning beats affects the turning angle $|\delta\phi|$ (Fig. 3a), and we find a linear increase of $(18 \pm 3)°$ per beat ($n = 7$ cells, 202 turning events, a total of 1,091 beats, always mean ± s.e.m. unless stated otherwise). This implies that larger turns take more time, and there are slight variations between different cells. This discreteness is further highlighted by distinct peaks in the frequency distribution of normalized $|\delta\phi|$ for different beat numbers (Fig. 3b, Supplementary Fig. 5 and Supplementary Section 3.3). Hence, the number of spinning beats determines the turning angle and hence the order of the polygon (Fig. 3c).

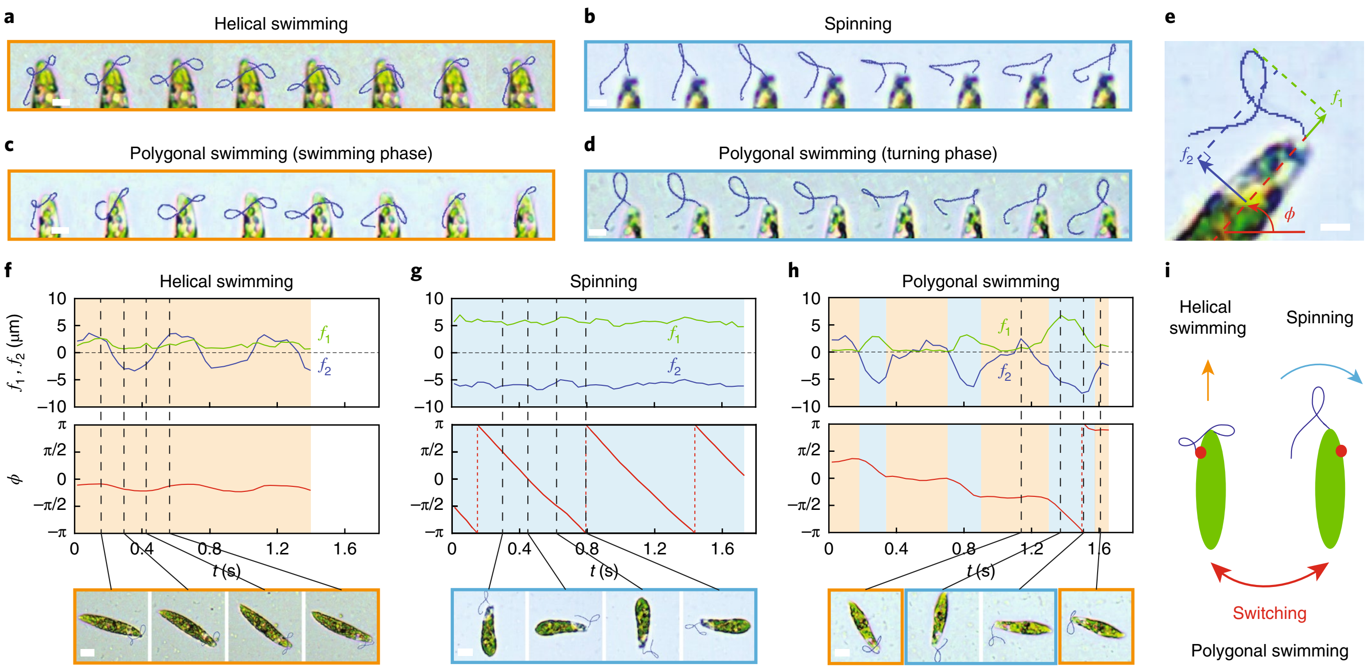

Fig. 2 | *Euglena* switches between two flagellar beating patterns to achieve the three behavioural states of helical swimming, polygonal swimming and spinning. a–d, Time-lapse images depicting representative flagellar beat patterns (traced in blue; 200 ms frame interval) for each behaviour; the orange and cyan box borders highlight helical versus spinning patterns. **e**, Flagellar beat patterns are quantified by f_1 (green) and f_2 (blue); ϕ measures cell orientation. **f–h**, Comparing f_1, f_2 and the rate of change of ϕ for all three behaviours reveals that the beat patterns for polygonal swimming closely resemble a periodic switching between helical and spinning behaviour ($n = 9$ cells, Supplementary Section 3.2). **i**, Polygonal swimming emerges from periodic switching between helical and spinning beat patterns. Scale bars, 5 μm.

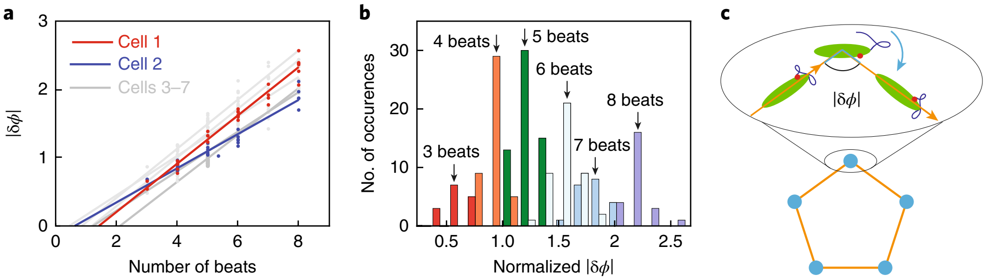

Fig. 3 | The number of spinning-type beats determines the turning angle and hence the order of the polygon. a, The turning angle $|\delta\phi|$ during the polygonal turning phase increases in a discrete manner proportional to the number of beats. Data for cell 1 and cell 2 are emphasized to show examples with two different slopes. **b**, A histogram of occurrences of normalized $|\delta\phi|$ versus beat number ($n = 7$ cells, Supplementary Section 3.3; bin width 0.32, always two samples from different beat numbers in the same bin, for visualization purposes with a small white gap between bins). **c**, Periodic turns give rise to quantized polygons, where $|\delta\phi|$ determines the order of the polygon.

Feedback model for light sensation and cell reorientation

Second, we turned to the cellular level to analyse the two-way feedback between light sensed by the eyespot and 3D cell reorientation with respect to the laboratory and body frames (Fig. 4a). In the laboratory frame ($\hat{\mathbf{x}}$, $\hat{\mathbf{y}}$, $\hat{\mathbf{z}}$), ϕ is defined as before, θ is the phase angle for the periodic helical trajectory due to the angular oscillation of amplitude ξ in the $\hat{\mathbf{x}}$–$\hat{\mathbf{y}}$ plane via $\xi = \xi sin(\theta)$, and the light stimulus $\mathbf{I}$ is parallel to $\hat{\mathbf{z}}$. In the body frame ($\hat{\mathbf{b}}_x$, $\hat{\mathbf{b}}_y$, $\hat{\mathbf{b}}_z$), we define $\hat{\mathbf{r}}$ (direction of maximal light sensitivity, which is assumed to align with the eyespot orientation $\hat{\mathbf{b}}_y$; see Supplementary Section 3.4 for generalizations), $\hat{\mathbf{u}}$ (swimming direction) and $\hat{\mathbf{p}}$ ('paw axis', see below). Cells swim at speed v along $\hat{\mathbf{u}}$, roll around $\hat{\mathbf{u}}$ at frequency ω (positive for anticlockwise as before) and turn around $\hat{\mathbf{p}}$. Instead of the 'roll–pitch–yaw' reference system, we substitute the last two components with a 'yitch–paw' vector, $K\hat{\mathbf{p}}$, where the body rotations perpendicular to the roll axis are fully described by the 'paw angle' α with respect to the eyespot (the unit 'paw vector' $\hat{\mathbf{p}}$ is perpendicular to the 'roll axis') and the 'yitch rate' K (defining the magnitude of rotation around $\hat{\mathbf{p}}$).

We consider a biophysical model that accounts for the reorientation feedback of *Euglena* in response to the detected light stimuli (see Supplementary Section 3.4 for generalizations): $K(t)$ depends on absolute light intensity $|\mathbf{I}|$ and light sensor orientation relative to the light ($\mathbf{I}\cdot\hat{\mathbf{r}}$), which is described by coupling constants K_a and K_d (for ambient and directional light components, respectively). We decompose $K(t)$ into $K_0(t)$ (intrinsic, light-independent reorientation rate), $K_1(t)$ (instantaneous signal strength) and $K_2(t)$ (receptor's adaptation to light). First, K_1 is given by:

$$K_1(t) = K_a\,|\mathbf{I}| + K_d\,(\mathbf{I}\cdot\hat{\mathbf{r}})\,\mathrm{H}(\mathbf{I}\cdot\hat{\mathbf{r}}) \tag{1}$$

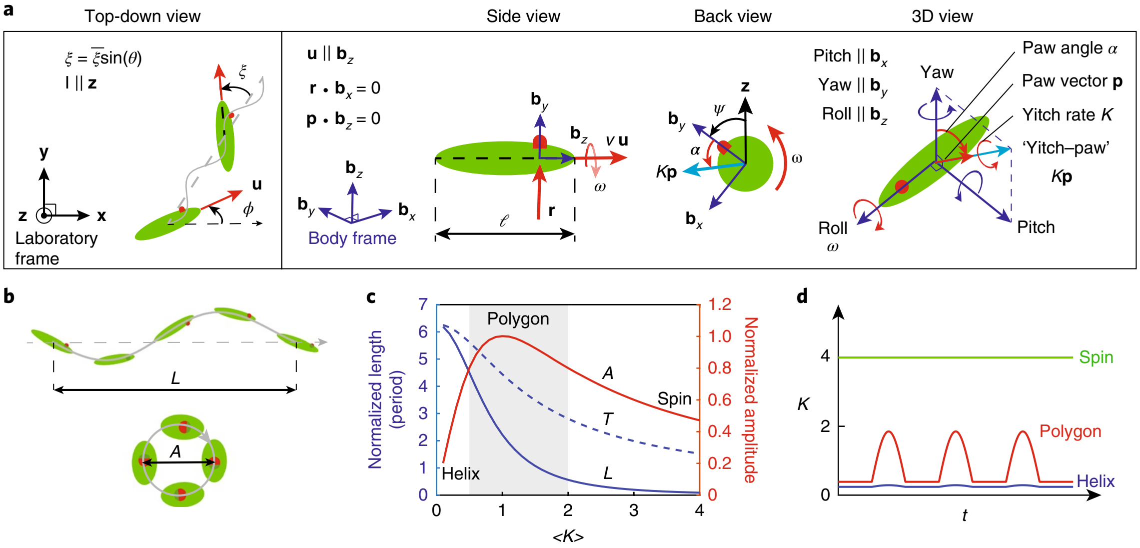

Fig. 4 | A biophysical model accounts for the reorientation feedback of *Euglena* in response to the detected light, capturing the transitions between the three behavioural states. a, A model schematic and parameter definitions; light stimulus **I** in the +$\hat{z}$ direction. The 'yitch-paw' vector, $K\hat{p}$, determines the feedback turning of cells with respect to the eyespot's vector $\hat{r}$ upon to the detected stimulus **I**. **b**, Side and front view of the helical paths generated by the model. (The size of the cell is reduced for visualization purposes.) **c**, Relations of A, L and T to $\langle K\rangle$ (average K over the half rolling cycle that **I** is detected by the photoreceptor), coloured lines and vertical axis correspond to each other. The grey region highlights polygonal swimming. **d**, $K(t)$ (without adaptation) in response to detected **I** for different behaviours.

The Heaviside function H accounts for directional shading by the eyespot. Next, $K_2(t)$ is given by:

$$K_2(t) = K_1(t) - \gamma \int_{-\infty}^{t} K_1(t')e^{-\gamma(t-t')}\mathrm{d}t' \qquad (2)$$

Here γ is the adaptation rate ($\gamma \ll \omega/(2\pi)$). Finally, $K(t)$ is given by:

$$K(t) = K_0 + K_2(t)H(K_2(t)) \qquad (3)$$

The Heaviside function ensures only activating signals. We nondimensionalize the system in space and time based on the body length ℓ and the inverse of the rolling frequency $1/\omega$, with v held constant (Fig. 4a). We define $\langle K\rangle$ as the average of $K(t)$ over the half rolling cycle that **I** is detected by the photoreceptor. $\alpha(\langle K\rangle)$ sets the direction of light-dependent turning (Fig. 4a), takes discrete values of $\alpha(\langle K\rangle < 3) = \alpha_1$ and $\alpha(\langle K\rangle \geq 3) = \alpha_2$, and does not adapt over time with light level.

Parameter exploration shows that this model can simulate all three behaviours and their dependencies on light intensity (Supplementary Section 3.5): for $\alpha \approx \pi$, cells perform helical swimming and polygonal swimming for $\langle K\rangle \approx 0$ and $\langle K\rangle \sim 1$–2, respectively. The simulated helical swimming is neither directed towards nor away from the light. Polygonal swimming is approximately confined to a plane perpendicular to the light vector, and the polygons have the same handedness as in Fig. 1a. If α is chosen to be ≈ 0, polygons have the opposite handedness. For all other α, cells eventually swim towards or away from light; that is, they do not stay in the same $\hat{\mathbf{z}}$-plane. For $\langle K\rangle \gtrsim 3$ and $\alpha \approx 3\pi/2$, cells spin perpendicular to the light, with the eyespot leading, as in Fig. 1c; for $\alpha \approx \pi/2$, the eyespot is on the other side. Other α values lead to spinning behaviour in planes that are not orthogonal to the light. We therefore set $\alpha_1 = \pi$ and $\alpha_2 = 3\pi/2$. Using these α values, we vary $K(t)$ and characterize the 3D helical trajectories by their amplitude A, helix length L and helix period T (Fig. 4b). With increasing $\langle K\rangle$, A first increases before it eventually decreases, while L and T both decrease monotonically (Fig. 4c). At large $\langle K\rangle$, spinning emerges as a zero-twist helix with small A, L and T. Polygonal swimming occurs as the light sensed by the photoreceptor is periodically blocked by the eyespot during the rolling cycle, thereby resulting in an 'on-and-off' signal in $K(t)$ (Fig. 4d). In contrast, in helical swimming and spinning, cells sense low and high light intensities at all times, respectively. These modelling results predict the importance of the changes in the detected light stimulus due to eyespot rolling in different behavioural states. In the following, we verify these predictions experimentally.

Phase relationships between eyespot and reorientation

For weak light intensities (<100 lx, $\mathbf{I} \approx O(10)^{-1}\hat{\mathbf{z}}$), the model predicts that the frequencies of body rolling and helical swimming are coupled, identical and phase locked (Fig. 5a(i) and Supplementary Video 5). We experimentally verified this by tracking ϕ and θ of helically swimming cells. We also tracked ψ, defined as the roll angle using the eyespot as a reference point (Fig. 4a) when observed from the top (that is, $-\hat{\mathbf{z}}$). We found a fixed phase relation between ψ and ϕ as well as ψ and θ (Fig. 5a(ii,iii)), in agreement with our model and recent work on *Euglena*[18] and other microswimmers[4,12]. Fitting experimental and theoretical results revealed that this phase relation is fixed at $\alpha = 3.32 \pm 0.07 \approx \pi$ ($n = 9$ cells, ≥3 periods, from similar plots as Fig. 5a(iii)).

For strong light intensities (>3,000 lx, $\mathbf{I} > 4\hat{\mathbf{z}}$), the model predicts that spinning behaviour occurs without rolling around the long axis (Fig. 5b(i) and Supplementary Video 6). We experimentally verified that the cells spin around their short axis in a plane perpendicular to the light, in either a clockwise or anticlockwise direction (experiments revealed no bias) when the light sensor saturates. In the experiments, cells did not appear to roll around their long axis (ψ = const) and we measured non-zero forward velocity (which is also observed in theory, Fig. 4b), while the orientation ϕ varies linearly with time (Fig. 5b(ii)). Fitting experimental and theoretical results revealed that the yitch rate was much larger than the rolling frequency ($\langle K\rangle \gg 1$) and $\alpha = 4.80 \pm 0.24 \approx 3\pi/2$ ($n = 7$ cells, ≥1.5 periods).

For intermediate light intensities (~1,000 lx, $\mathbf{I} \approx 1$–$2\hat{\mathbf{z}}$), the model predicts that polygonal swimming behaviours emerge due to periodic shading of the eyespot to the light stimulus (Fig. 5c(i) and

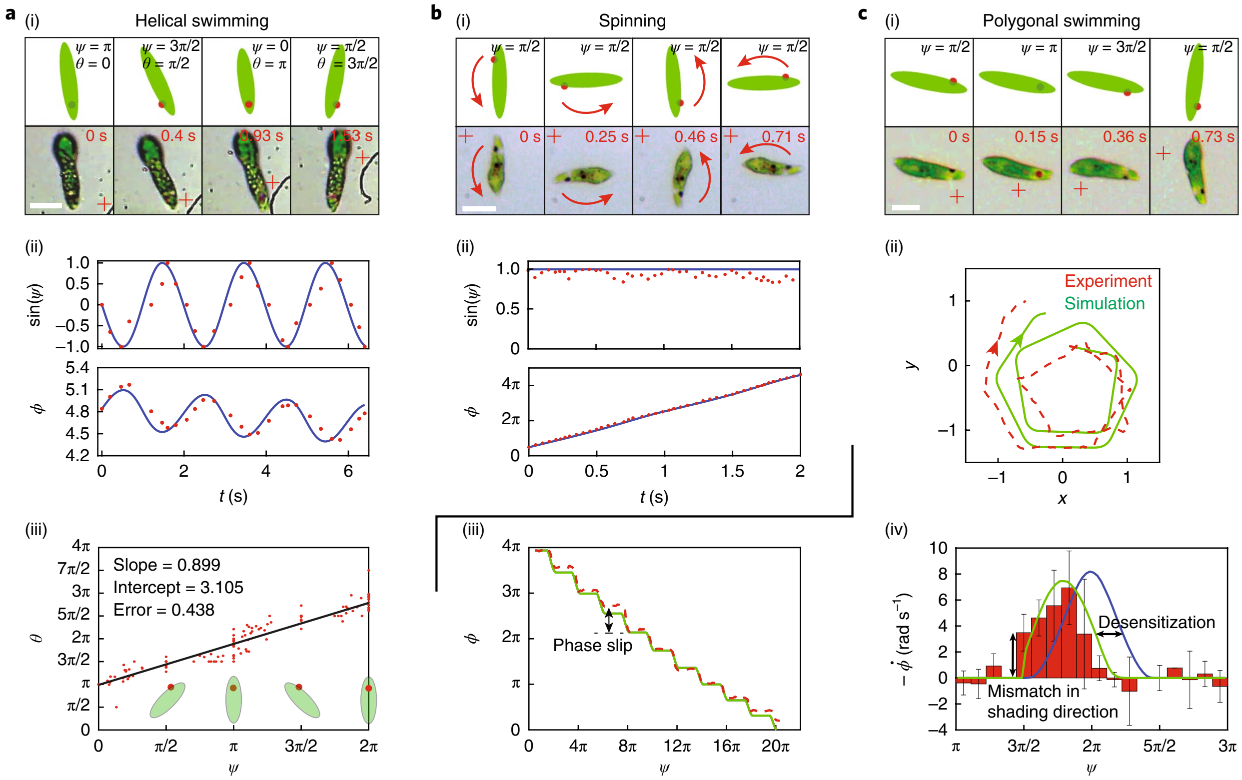

Fig. 5 | Model simulations and experiments reveal distinct phase relations between eyespot and cell orientation for the three different behavioural states. a–c, (i) Time-lapse images of eyespot versus cell orientation; simulation (top) versus experiment (bottom); the plus symbol marks the same location within the image sequence; scale bar, 15 µm. (ii–iv) Simulation (blue lines from the model given by equations (1)–(3); or green lines from a more general model defined in Supplementary Section 3.4); experiment (red dots). **a**, Helical swimming. (i) The cell orientation oscillates sideways; the eyespot rolls around the long axis. (ii) sin($\psi(t)$) and $\phi(t)$. (iii) Constant phase relation ψ versus θ, linear fit. **b**, Spinning. (i) The cell continuously spins around the short axis; the eyespot does not roll. (ii) sin($\psi(t)$) and $\phi(t)$. **c**, Polygonal swimming. (i) The cell orientation alternates between straight swimming and sharp sideways turning; the eyespot always rolls around the long axis. (ii) Polygonal spiral swimming path due to adaptation (ℓ scaled to 1). (iii) $\phi(t)$ versus $\psi(t)$, note the phase slip of ϕ during polygonal turns. (iv) The angular velocity distribution $-\dot{\phi}(t)$ versus $\psi(t)$ reveals the effects of adaptation and desensitization on sideways turning; the error bars denote experimental s.d.; the blue and green lines show the mean $-\dot{\phi}$ obtained from the simulations. See Supplementary Sections 3.4–3.7 for model parameters and additional details.

Supplementary Video 7). The cells sense the light stimulus for only part of the rolling cycle due to eyespot shading; that is, they turn sideways (orthogonal to the light direction) whenever the light is detected, and they swim in a helix whenever the light is not detected. This process then repeats periodically and a polygon emerges. We experimentally verified this and observed clockwise polygonal trajectories that occur due to the inherent symmetry breaking from handedness of rolling and directionality of the light ($+\hat{\mathbf{z}}$ direction). This polygonal path is actually not completely planar but slowly moves along the light direction (approximately 1 body length for 5–10 rolling cycles in simulations; in experiments, the cells swim out of focus slowly due to this motion). Fitting experimental and theoretical results revealed that $\alpha = 3.18 \pm 0.12 \approx \pi$ ($n = 9$ cells, ≥3 periods).

Since the model accounts for adaptation (equation (2)), it is predicted that the diameter of the polygonal path increases in size over time (Fig. 5c(ii) and Supplementary Section 3.6). The corresponding polygonal spirals were found experimentally (Fig. 5c(ii)). For the cell shown in Fig. 5c, we obtained an adaption timescale of ~2 min, after which it transitioned to helical motion. The polygonal turns manifest themselves as 'phase slips' between ψ and ϕ (Fig. 5c(iii)). However, we also observed that these cells finished the turning phase much faster than predicted by the model given by equations (1)–(3) (blue lines versus red bars in Fig. 5c(iv)). A better match can be achieved with a more general model that accounts for a mismatch in the sensor's vector and shading direction as well as for short-time desensitization (green line in Fig. 5c(ii–iv), and Supplementary Sections 3.4 and 3.6). Thus, we show that the polygonal behaviour can be explained by the cell sensing a strong, temporary light stimulus that causes turning, and where the sensor adapts over time.

Phototactic strategies and anomalous diffusion

Third, we investigated the utility of these three behaviours for phototactic navigation strategies over longer timescales and length scales (Fig. 6). Using an image projector coupled into the microscope, we generated different spatially structured light landscapes that were either constant in time or were suddenly switched on[25,33] (Fig. 1e, Supplementary Fig. 1 and Supplementary Section 2.3). We observed the resulting trajectories (Fig. 6a–c, top). (1) When cells ($n = 27$) coming from low light encounter a step-up to higher light intensity, polygonal swimming or localized spinning occurs, making the cells turn around and avoid the light 'barrier' (Fig. 6a and Supplementary Video 8). (2) When suddenly imposing a strong, spatially homogeneous light onto cells ($n = 10$) that had previously been at low light, these cells initially spin and then swim in polygons of increasing order (eventually intermittently skipping the turning phases) and thereby increase their 'search radius' before ultimately escaping into darker regions and switching back to pure helical motion (Fig. 6b and Supplementary Video 9). (3) When cells ($n = 15$) under low light are suddenly exposed to a spatial light

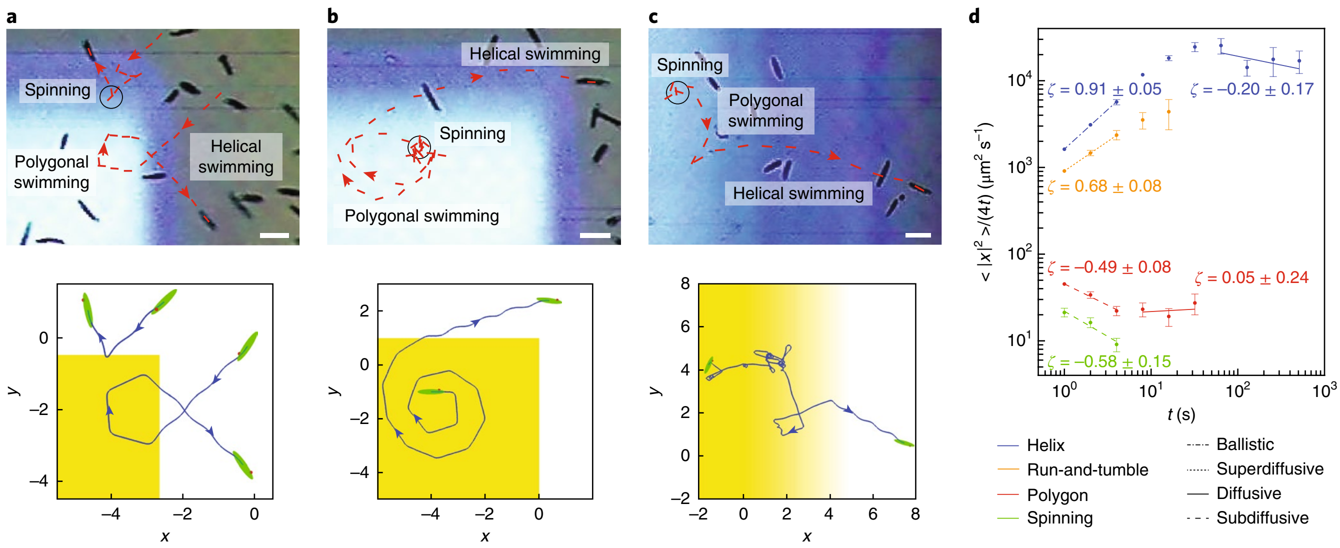

Fig. 6 | *Euglena* accomplish versatile phototaxis strategies including edge avoidance and gradient descent, through behavioural state switching and selection of different anomalous diffusion types. a, *Euglena* encountering a sudden step-up in light intensity take multiple polygonal turns or directly spin around, performing edge avoidance (duration: 5 s). **b**, *Euglena* exposed to a sudden increase in light intensity initially spin before transitioning to polygonal paths of increasing order, performing a spiral search with increasing radius until the edge of the light field is encountered and ballistic helical motion sets in (duration: 21 s). **c**, *Euglena* cells exposed to a spatial light gradient switch between spinning, polygonal motion and helical swimming in a light-intensity-dependent matter, performing a biased 'run-and-tumble' towards darker regions (duration: 7 s). Bottom rows in **a–c**: corresponding model simulations, ℓ scaled to 1 (Supplementary Section 3.7). **d**, Log-log plot of $\langle |x|^2 \rangle/(4t)$ for different behavioural states over time t. Different forms of anomalous diffusion feature different slopes (that is, $\zeta = \varepsilon - 1$): subdiffusive ($-1 < \zeta < 1$), diffusive ($\zeta \sim 0$), superdiffusive ($\zeta > 0$) and ballistic ($\zeta \sim 1$). $n \geq 10$ cells for all cases; error bars are s.e.m. (sometimes smaller than the marker); slopes for the various linear fits are reported as mean and s.e.m. (see Supplementary Sections 3.9 and 3.10 for more detail on the cell number and sampling method). Scale bars, 50 μm.

gradient, they alternate between spinning, polygonal swimming and helical swimming, thereby executing a biased random walk down the light gradient (reminiscent of bacterial 'run-and-tumble'[2]) (Fig. 6c and Supplementary Video 10), and where the variation of $\dot{\phi}$ decreases accordingly (Supplementary Figs. 10 and 11). All of these strategies are captured in simulations with the model (Fig. 6a–c, bottom, and Supplementary Videos 11–13).

We quantitatively characterized these behaviours (Fig. 1a–c) and strategies (Fig. 6a–c) in terms of type and magnitude of anomalous diffusion as defined by $\langle |x|^2 \rangle = 4Dt^{\varepsilon}$, where D and ε are the generalized diffusion constant and anomalous diffusion exponent, respectively ($\varepsilon = 1$ and $\varepsilon = 2$ for normal diffusion and ballistic motion, respectively)[38,39]. We introduce $\zeta = \varepsilon - 1$ to conveniently represent the slopes in the log–log plot of $\langle |x|^2 \rangle/(4t)$ (normal diffusion constant in 2D) for the different scenarios over time t (Fig. 6d and Supplementary Sections 3.9 and 3.10). (1) Spinning leads to subdiffusive behaviour ($\zeta = -0.58 \pm 0.15$; <0, $P < 0.01$) as the small yet non-zero forward velocity makes the cell swim in small circles; after >10 s cells often stop spinning. (2) Pure helical swimming leads to nearly ballistic motion with $v = 78 \pm 6\,\mu m\,s^{-1}$ ($\zeta = 0.91 \pm 0.05$; not significantly different from 1, $P < 0.01$). Over longer times of ~1 min, the behaviour becomes diffusive ($\zeta = -0.20 \pm 0.17$; not significantly different from 0, $P < 0.01$) with $D = 18{,}500 \pm 1{,}600\,\mu m^2\,s^{-1}$. (3) Polygonal swimming exhibits subdiffusive behaviour at short times (<10 s) due to the looping motion ($\zeta = -0.49 \pm 0.08$; <0, $P < 0.01$), while over longer times (>10 s) the cells increase their search radius (Fig. 6b) and transition to normal diffusion ($\zeta = 0.05 \pm 0.24$, $P < 0.01$) with $D = 17 \pm 4\,\mu m^2\,s^{-1}$. After >1 min, cells eventually transition into helical swimming and follow scenario (2). (4) For run-and-tumble in the light gradient (Fig. 6c), cells exhibit superdiffusive behaviour over the first ~10–20 s given stochastic switching between helical, polygonal and spinning behaviours ($\zeta = 0.68 \pm 0.08$;>0, $P < 0.01$); after escape from the light field, they transition to scenario (2). Hence, *Euglena* select between ballistic motion and different forms of anomalous diffusion (normal, subdiffusive and superdiffusive), and can, over longer timescales, adjust their effective diffusion constants by multiple orders of magnitude (Fig. 6d), ultimately allowing these cells to adapt their search strategy to the relevant length scale in complex light environments to perform edge avoidance, local search and gradient descent.

Outlook

Finally, we note that navigation and search perpendicular to the light vector is relevant for photosynthesis and avoiding ultraviolet damage[5,35,40]. For example, cells might swim into a bright region from under an obstacle (Fig. 6a), or the sun might appear from behind a cloud (Fig. 6b,c). The values we experimentally obtained for α suggest that under these conditions *Euglena* are tuned to perform initially phototaxis perpendicular to the light vector. While cells cannot instantaneously discriminate between localized or global causes of these light intensity changes, the feedback-control loop between flagellar beat patterns, the cells' rolling phase, stimulus detection, reorientation response and longer-term adaptation enables cells to select the optimal response (Fig. 6a–c): typically, cells first perform a localized search via spinning at the length scale that cells swim in one roll (that is, 50–100 μm), followed by a steady increase in search radius through polygonal motion, then intermittently transitioning between polygon and helix, ultimately reaching the ballistic motion for the pure helix. Note that these processes bind together timescales and length scales from milliseconds to minutes and micrometres to millimetres, respectively. Future work may elucidate the relationship between phototaxis perpendicular versus along the light vector[5,6,27,37], map out the various 3D flagellar beating patterns in detail[18], directly relate the hydrodynamics of these patterns to K and α, and clarify the signalling transduction pathway[5] from light sensation (including adaptation) to flagellar beat selection. The presented insights might generalize to other natural microswimmers, enlighten the self-organized behaviours of microswimmer suspensions[41–43] and inform the design and control of light-guided synthetic microswimmers[33,44–46].

Reporting Summary. Further information on experimental design is available in the Nature Research Reporting Summary linked to this article.

Received: 31 March 2018; Accepted: 15 August 2018;

References

1. Miller, M. B. & Bassler, B. L. Quorum sensing in bacteria. *Annu. Rev. Microbiol.* **55**, 165–199 (2001).
2. Berg, H. C. & Brown, D. A chemotaxis in *Escherichia coli* analysed by three-dimensional tracking. *Nature* **239**, 500–504 (1972).
3. Friedrich, B. M. & Jülicher, F. Chemotaxis of sperm cells. *Proc. Natl Acad. Sci. USA* **104**, 13256–13261 (2007).
4. Drescher, K., Goldstein, R. E. & Tuval, I. Fidelity of adaptive phototaxis. *Proc. Natl Acad. Sci. USA* **107**, 11171–11176 (2010).
5. Diehn, B. Phototaxis and sensory transduction in *Euglena*. *Science* **181**, 1009–1015 (1973).
6. Häder, D. Simulation of phototaxis in the flagellate *Euglena gracilis*. *J. Biol. Phys.* **19**, 95–108 (1993).
7. Machemer, H. Swimming sensory cells: electrical membrane parameters, receptor properties and motor control in ciliated protozoa. *Verh. Dtsch. Zool. Ges.* **1977**, 86–110 (1977).
8. Ogawa, N., Oku, H., Hashimoto, K. & Ishikawa, M. A physical model for galvanotaxis of *Paramecium* cell. *J. Theor. Biol.* **242**, 314–328 (2006).
9. Riedel-Kruse, I. H., Chung, A. M., Dura, B., Hamilton, A. L. & Lee, B. C. Design, engineering and utility of biotic games. *Lab Chip* **11**, 14–22 (2011).
10. Kantsler, V., Dunkel, J., Blayney, M. & Goldstein, R. E. Rheotaxis facilitates upstream navigation of mammalian sperm cells. *eLife* **3**, e02403 (2014).
11. Arrieta, J., Barreira, A., Chioccioli, M., Polin, M. & Tuval, I. Phototaxis beyond turning: persistent accumulation and response acclimation of the microalga *Chlamydomonas reinhardtii*. *Sci. Rep.* **7**, 3447 (2017).
12. Schaller, K., David, R. & Uhl, R. How *Chlamydomonas* keeps track of the light once it has reached the right phototactic orientation. *Biophys. J.* **73**, 1562–1572 (1997).
13. Bennett, R. R. & Golestanian, R. A steering mechanism for phototaxis in *Chlamydomonas*. *J. R. Soc. Interface* **12**, 20141164 (2015).
14. Sartori, P., Geyer, V. F., Scholich, A., Jülicher, F. & Howard, J. Dynamic curvature regulation accounts for the symmetric and asymmetric beats of Chlamydomonas flagella. *eLife* **5**, e13258 (2016).
15. Leptos, K. C., Chioccioli, M., Furlan, S., Pesci, A. I. & Goldstein, R. E. An adaptive flagellar photoresponse determines the dynamics of accurate phototactic steering in *Chlamydomonas*. Preprint at https://www.biorxiv.org/content/early/2018/02/17/254714 (2018).
16. Hill, N. A. & Vincent, R. V. A simple model and strategies for orientation in phototactic microorganisms. *J. Theor. Biol.* **163**, 223–235 (1993).
17. Giometto, A., Altermatt, F., Maritan, A., Stocker, R. & Rinaldo, A. Generalized receptor law governs phototaxis in the phytoplankton *Euglena gracilis*. *Proc. Natl Acad. Sci. USA* **112**, 7045–7050 (2015).
18. Rossi, M., Cicconofri, G., Beran, A., Noselli, G. & DeSimone, A. Kinematics of flagellar swimming in *Euglena gracilis*: Helical trajectories and flagellar shapes. *Proc. Natl Acad. Sci. USA* **114**, 13085–13090 (2017).
19. Wan, K. Y. & Goldstein, R. E. Time irreversibility and criticality in the motility of a flagellate microorganism. *Phys. Rev. Lett.* **121**, 058103 (2018).
20. Polin, M., Tuval, I., Drescher, K., Gollub, J. P. & Goldstein, R. E. *Chlamydomonas* swims with two "gears" in a eukaryotic version of run-and-tumble locomotion. *Science* **325**, 487–490 (2009).
21. Lauga, E., DiLuzio, W. R., Whitesides, G. M. & Stone, H. A. Swimming in circles: motion of bacteria near solid boundaries. *Biophys. J.* **90**, 400–412 (2006).
22. Ozasa, K. et al. Temporal change of photophobic step-up responses of *Euglena gracilis* investigated through motion analysis. *PLoS One* **12**, e0172813 (2017).
23. Nichols, K. M., Jacklet, A. & Rikmenspoel, R. Effects of Mg^{2+} and Ca^{2+} on photoinduced *Euglena* flagellar responses. *J. Cell. Biol.* **84**, 355–363 (1980).
24. Arroyo, M., Heltai, L., Millán, D. & DeSimone, A. Reverse engineering the euglenoid movement. *Proc. Natl Acad. Sci. USA* **109**, 17874–17879 (2012).
25. Lee, S. A. et al. Trap it!: a playful human–biology interaction for a museum installation. In *Proc. 33rd Annual ACM Conference on Human Factors in Computing Systems* 2593–2602 (ACM, 2015).
26. Cira, N. J. et al. A biotic game design project for integrated life science and engineering education. *PLoS Biol.* **13**, e1002110 (2015).
27. Hossain, Z. et al. Interactive and scalable biology cloud experimentation for scientific inquiry and education. *Nat. Biotechnol.* **34**, 1293–1298 (2016).
28. Hossain, Z. et al. Design guidelines and empirical case study for scaling authentic inquiry-based science learning via open online courses and interactive biology cloud labs. *Int. J. Artif. Intell. Educ.* https://doi.org/10.1007/s40593-017-0150-3 (2017).
29. Kim, H. et al. LudusScope: accessible interactive smartphone microscopy for life-science education. *PLoS One* **11**, e0162602 (2016).
30. Morimoto, K. & Takemura, A. Developing teaching materials using LED for a phototaxis in *Euglena*. *J. Res. Sci. Educ.* **45**, 73–77 (2005).
31. Ozasa, K., Lee, J., Song, S., Hara, M. & Maeda, M. Gas/liquid sensing via chemotaxis of *Euglena* cells confined in an isolated micro-aquarium. *Lab Chip* **13**, 4033–4039 (2013).
32. Ozasa, K., Lee, J., Song, S., Hara, M. & Maeda, M. Two-dimensional optical feedback control of *Euglena* confined in closed-type microfluidic channels. *Lab Chip* **11**, 1933–1940 (2011).
33. Lam, A. T. et al. Device and programming abstractions for spatiotemporal control of active micro-particle swarms. *Lab Chip* **17**, 1442–1451 (2017).
34. Krajvovic, J., Vesteg, M. & Schwartzbach, S. D. Euglenoid flagellates: A multifaceted biotechnology platform. *J. Biotechnol.* **202**, 135–145 (2015).
35. Leander, B. S., Lax, G., Karnkowska, A. & Simpson, A. G. B. *Handbook of the Protists* 1047–1088 (Springer, Cham, 2017).
36. Ascoli, C., Barbi, M., Frediani, C. & Mure, A. Measurements of *Euglena* motion parameters by laser light scattering. *Biophys. J.* **24**, 585–599 (1978).
37. Ogawa, T. et al. The flux of *Euglena gracilis* cells depends on the gradient of light intensity. *PLoS One* **11**, e0168114 (2016).
38. Metzler, R. & Klafter, J. The random walk's guide to anomalous diffusion: a fractional dynamics approach. *Phys. Rep.* **339**, 1–77 (2000).
39. Metzler, R., Jeon, J.-H., Cherstvy, A. G. & Barkai, E. Anomalous diffusion models and their properties: non-stationarity, non-ergodicity, and ageing at the centenary of single particle tracking. *Phys. Chem. Chem. Phys.* **16**, 24128–24164 (2014).
40. Häder, D.-P. & Griebenow, K. Orientation of the green flagellate, *Euglena gracilis*, in a vertical column of water. *FEMS Microbiol. Lett.* **53**, 159–167 (1988).
41. Shoji, E., Nishimori, H., Awazu, A., Izumi, S. & Iima, M. Localized bioconvection patterns and their initial state dependency in *Euglena gracilis* suspensions in an annular container. *J. Phys. Soc. Jpn* **83**, 043001 (2014).
42. Wioland, H., Woodhouse, F. G., Dunkel, J. & Goldstein, R. E. Ferromagnetic and antiferromagnetic order in bacterial vortex lattices. *Nat. Phys.* **12**, 341–345 (2016).
43. Riedel, I. H., Kruse, K. & Howard, J. A self-organized vortex array of hydrodynamically entrained sperm cells. *Science* **309**, 300–303 (2005).
44. Dai, B. et al. Programmable artificial phototactic microswimmer. *Nat. Nanotech.* **11**, 1087–1092 (2016).
45. Lozano, C., Ten Hagen, B., Löwen, H. & Bechinger, C. Phototaxis of synthetic microswimmers in optical landscapes. *Nat. Commun.* **7**, 12828 (2016).
46. Palacci, J., Sacanna, S., Steinberg, A. P., Pine, D. J. & Chaikin, P. M. Living crystals of light-activated colloidal surfers. *Science* **339**, 936–940 (2013).

Acknowledgements

We thank members of the Riedel-Kruse laboratory, B. Friedrich, J. Dunkel, N. Ouellette and A. Macdonald. This work was supported by NSF grant no. 1324753, the Stanford Discovery Innovation Fund and the Croucher Foundation (through a postdoctoral fellowship to A.C.H.T.).

Author contributions

A.C.H.T. and I.H.R.-K. were responsible for the project idea, the theory and manuscript preparation; A.C.H.T. was responsible for the modelling, the experiments and data analysis (except Fig. 6: A.C.H.T. and A.T.L.).

Competing interests

The authors declare no competing interests.

Additional information

Supplementary information is available for this paper at https://doi.org/10.1038/s41567-018-0277-7.

Reprints and permissions information is available at www.nature.com/reprints.

Correspondence and requests for materials should be addressed to I.H.R.

nature research

Corresponding author(s): *Double-blind peer review submissions: write DBPR and your manuscript number here instead of author names.*

☒ Initial submission ☐ Revised version ☐ Final submission

Editorial Policy Checklist

This form is used to ensure compliance with Nature Research editorial policies related to research ethics and reproducibility. For further information, please see our Authors & Referees site. All relevant questions on the form must be answered.

Competing interests

Policy information about competing interests

Competing interests declaration

In the interest of transparency and to help readers form their own judgements of potential bias, Nature Research journals require authors to declare any competing financial and/or non-financial interest in relation to the work described in the submitted manuscript.

☒ No, I declare that the authors have no competing financial or non-financial interests as defined by Nature Research.

☐ Yes, I declare that the authors have a competing interest as defined by Nature Research

Data availability

Policy information about availability of data

Data availability statement

All manuscripts must include a data availability statement. This statement should provide the following information, where applicable:

- Accession codes, unique identifiers, or web links for publicly available datasets
- A list of figures that have associated raw data
- A description of any restrictions on data availability

☒ A full data availability statement is included in the manuscript.

Mandated accession codes (where applicable)

Confirm that all relevant data are deposited into a public repository and that accession codes are provided.

☐ All relevant accession codes are provided ☐ Accession codes will be available before publication ☐ No data with mandated deposition

Data presentation

Image integrity

☒ Confirm that all images comply with our image integrity policy.

Unprocessed data must be provided upon request. Please double-check figure assembly to ensure that all panels are accurate (e.g. all labels are correct, no inadvertent duplications have occurred during preparation, etc.).

Data distribution

Present data in a format that shows data distribution (dot-plots or box-and-whisker plots).

Define all box-plot elements (e.g. center line, median; box limits, upper and lower quartiles; whiskers, 1.5x interquartile range; points, outliers).

If using bar graphs, overlay the corresponding dot plots.

☒ Confirm that all data presentation meets these requirements and that individual data points are shown.

Specific policy considerations

Some types of research require additional policy disclosures. Please indicate whether these apply to your study. If you are not certain, please read the appropriate section before selecting a response.

Does not apply	Involved in the study	
☐	☒	Custom software or computer code
☒	☐	Macromolecular structural data
☒	☐	Research animals and/or animal-derived materials that require ethical approval
☒	☐	Human research participants
☒	☐	Clinical data

▸ Code availability

Policy information about availability of computer code

Code availability statement

For all studies using custom code, the Methods section must include a statement under the heading "Code availability" describing how readers can access the code, including any access restrictions.

☒ A full code availability statement is included in the manuscript

---

I certify that all the above information is complete and correct.

Typed signature Ingmar H. Riedel-Kruse

Date Apr 24, 2018

nature research

Corresponding author(s): Ingmar Riedel-Kruse

Reporting Summary

Nature Research wishes to improve the reproducibility of the work that we publish. This form provides structure for consistency and transparency in reporting. For further information on Nature Research policies, see Authors & Referees and the Editorial Policy Checklist.

Statistical parameters

When statistical analyses are reported, confirm that the following items are present in the relevant location (e.g. figure legend, table legend, main text, or Methods section).

n/a	Confirmed	
☐	☒	The exact sample size (*n*) for each experimental group/condition, given as a discrete number and unit of measurement
☐	☒	An indication of whether measurements were taken from distinct samples or whether the same sample was measured repeatedly
☐	☒	The statistical test(s) used AND whether they are one- or two-sided *Only common tests should be described solely by name; describe more complex techniques in the Methods section.*
☐	☒	A description of all covariates tested
☐	☒	A description of any assumptions or corrections, such as tests of normality and adjustment for multiple comparisons
☐	☒	A full description of the statistics including central tendency (e.g. means) or other basic estimates (e.g. regression coefficient) AND variation (e.g. standard deviation) or associated estimates of uncertainty (e.g. confidence intervals)
☒	☐	For null hypothesis testing, the test statistic (e.g. *F*, *t*, *r*) with confidence intervals, effect sizes, degrees of freedom and *P* value noted *Give P values as exact values whenever suitable.*
☒	☐	For Bayesian analysis, information on the choice of priors and Markov chain Monte Carlo settings
☒	☐	For hierarchical and complex designs, identification of the appropriate level for tests and full reporting of outcomes
☒	☐	Estimates of effect sizes (e.g. Cohen's *d*, Pearson's *r*), indicating how they were calculated
☐	☒	Clearly defined error bars *State explicitly what error bars represent (e.g. SD, SE, CI)*

Our web collection on statistics for biologists may be useful.

Software and code

Policy information about availability of computer code

Data collection	The cell data were collected by manual tracking in the open source software ImageJ.
Data analysis	The data were analyzed with customized codes in MATLAB 2017b.

For manuscripts utilizing custom algorithms or software that are central to the research but not yet described in published literature, software must be made available to editors/reviewers upon request. We strongly encourage code deposition in a community repository (e.g. GitHub). See the Nature Research guidelines for submitting code & software for further information.

Data

Policy information about availability of data

All manuscripts must include a data availability statement. This statement should provide the following information, where applicable:

- Accession codes, unique identifiers, or web links for publicly available datasets
- A list of figures that have associated raw data
- A description of any restrictions on data availability

The datasets generated during and analyzed during the current study are available from the corresponding author on reasonable request.

Field-specific reporting

Please select the best fit for your research. If you are not sure, read the appropriate sections before making your selection.

☒ Life sciences ☐ Behavioural & social sciences ☐ Ecological, evolutionary & environmental sciences

For a reference copy of the document with all sections, see nature.com/authors/policies/ReportingSummary-flat.pdf

Life sciences study design

All studies must disclose on these points even when the disclosure is negative.

Sample size	The sample size for each experiment have been described in the article and supplementary materials. The sample size was determined by the estimation of the statistical differences between different data set, which we have indicated as the error bars in the figures and text.
Data exclusions	No data were excluded from the analysis.
Replication	We have repeated each experiment and cell behavior we reported in the article with the number of trials/samples described in the paper. We also provided the guidelines of the experiments, as well as important statistics and data for the readers to reproduce the experimental results.
Randomization	The samples were allocated randomly in our experiments. The samples were obtained from several shipments from Carolina Biological. The experiments were carried out with several different cell cultures, with experiments on each culture repeated on different days and times.
Blinding	Blinding was not relevant to our study as we were treating microorganisms instead of humans.

Reporting for specific materials, systems and methods

Materials & experimental systems

n/a	Involved in the study
☒	☐ Unique biological materials
☒	☐ Antibodies
☒	☐ Eukaryotic cell lines
☒	☐ Palaeontology
☒	☐ Animals and other organisms
☒	☐ Human research participants

Methods

n/a	Involved in the study
☒	☐ ChIP-seq
☒	☐ Flow cytometry
☒	☐ MRI-based neuroimaging